Research Square

Preprints are preliminary reports that have not undergone peer review.
They should not be considered conclusive, used to inform clinical practice,
or referenced by the media as validated information.

Computational identification of Glycyrrhiza glabra-derived Semilicoisoflavone B and Licoisoflavone B as dual-target inhibitors of Ebola virus proteins

Fahad Fardin
Jahangirnagar University
Md. Al-Amin
Jagannath University
Abir Hossain
University of Dhaka
Moshammat Nasrin Akter
Gazipur Agricultural University
Md. Shohel Hossain
Gono Bishwabidyalay
M. Nazmul Hoque
nazmul90@gau.edu.bd

Gazipur Agricultural University

Article

Keywords: Ebola virus, VP40 matrix protein, Nucleoprotein, Glycyrrhiza glabra, Phytocompounds, Molecular docking, Dynamics simulation, Antiviral therapeutics

Posted Date: April 6th, 2026

DOI: https://doi.org/10.21203/rs.3.rs-9179366/v1

License: This work is licensed under a Creative Commons Attribution 4.0 International License.
Read Full License

Additional Declarations: No competing interests reported.

Computational identification of *Glycyrrhiza glabra*-derived Semilicoisoflavone B and Licoisoflavone B as dual-target inhibitors of Ebola virus proteins

Fahad Fardin [1#], Md. Al-Amin [2], Abir Hossain [3], Moshammat Nasrin Akter [4], Md. Shohel Hossain[5], M. Nazmul Hoque[6#]

[1] Department of Pharmacy, Jahangirnagar University, Dhaka, 1342, Bangladesh

[2] Department of Chemistry, Jagannath University, Dhaka 1100, Bangladesh

[3] Department of Microbiology, University of Dhaka, Dhaka, 1342, Bangladesh

[4] Department of Entomology, Gazipur Agricultural University, Gazipur 1706, Bangladesh

[5] Department of Pharmacy, Gono Bishwabidyalay, Savar 1344, Dhaka, Bangladesh.

[6] Molecular Biology and Bioinformatics Laboratory, Department of Gynecology, Obstetrics and Reproductive Health, Gazipur Agricultural University, Gazipur 1706, Bangladesh

[#] **Correspondence to:** Fahad Fardin, Email: fahad.stu20171@juniv.edu and M. Nazmul Hoque, Email: nazmul90@gau.edu.bd

Abstract

Ebola virus disease (EVD) is a life-threatening zoonotic infection caused by the Ebola virus (EBOV), characterized by high mortality rates and persistent global health concern, with no FDA-approved small-molecule therapeutics currently available. This study investigated *Glycyrrhiza glabra* phytochemicals as promising dual-target inhibitors of two essential EBOV proteins: matrix protein VP40 and nucleoprotein (NP). An integrated *in-silico* approach comprising molecular docking, ADMET profiling, 100 ns molecular dynamics simulations, principal component analysis, and density functional theory calculations was employed. Virtual screening of 408 phytocompounds identified two *G. glabra* -derived phytocompounds, Semilicoisoflavone B and Licoisoflavone B, as promising candidates, exhibiting superior binding affinities (VP40: −10.6 to −9.7 kcal/mol; NP: −9.2 to −8.8 kcal/mol) compared to control ligands Laurifolin and Licochalcone A. Both phytocompounds were identified as promising inhibitors, exhibiting strong binding affinity for both target proteins and favorable pharmacokinetics. Molecular dynamics simulations confirmed stable protein-ligand interactions, with Semilicoisoflavone B showing exceptional affinity for VP40 ($\Delta G = -129.21$ kcal/mol). PCA revealed constrained conformational dynamics, while density functional theory analysis demonstrated favorable electronic properties including narrow HOMO-LUMO gaps (3.69–4.21 eV). These findings suggest Semilicoisoflavone B and Licoisoflavone B as promising dual-target inhibitors of the VP40 and NP of the EBOV; however, further *in-vitro* and *in-vivo* studies are necessary to evaluate their therapeutic efficacy.

Keywords

Ebola virus; VP40 matrix protein; Nucleoprotein; *Glycyrrhiza glabra*; Phytocompounds; Molecular docking; Dynamics simulation; Antiviral therapeutics

Introduction

Ebola virus disease (EVD) is a severe and often lethal illness that has emerged as a significant global health concern, particularly in low- and middle-income countries (LMICs) of Africa, due to its rapid transmission and high mortality rate [1,2]. Ebola virus (EBOV) belongs to the *Orthoebolavirus* genus within the *Filoviridae* family and possesses a non-segmented, negative-strand RNA genome that encodes glycoproteins (GP), nucleoprotein (NP), RNA-dependent RNA polymerase, and three viral proteins (VP24, VP30, and VP40) [3]. The disease manifests with severe clinical manifestations, including hemorrhagic fever, multi-organ failure, and potential neurological complications [4]. Furthermore, an emerging condition termed "post-Ebola virus disease syndrome" has been characterized by inflammatory and autoimmune disorders, including rheumatoid arthritis, uveitis, and systemic lupus erythematosus [5]. EVD was first identified in 1976 during simultaneous outbreaks in northern Zaire (now the Democratic Republic of Congo) and southern Sudan [6]. Since its discovery, more than 30 outbreaks have occurred, resulting in approximately 15,350 deaths [7,8]. The clinical practice guideline for EVD treatment was published in 2022, and two monoclonal antibody-based therapies (Inmazeb and Ebanga) have received regulatory approval [9,10]. Despite these advances and notable progress in outbreak management, therapeutic options remain severely limited [11], and no FDA-approved small-molecule drugs are currently available for EVD treatment.

The EBOV life cycle depends on the coordinated function of its structural proteins. Nucleoprotein (NP) represents the most abundant structural protein, facilitating the encapsidation of genomic RNA and the formation of the ribonucleoprotein complex (RNP), which is essential for viral transcription and replication [12,13]. The crystal structure of the NP core domain (PDB ID: 4Z9P) has provided valuable insights into its assembly mechanism and potential drug-targeting sites [14].

Conversely, the matrix protein VP40 is the primary driver of matrix assembly and viral budding, as it can independently assemble filamentous virus-like particles (VLPs) in mammalian cells [15]. The structural rearrangement of VP40 (PDB ID: 4LDB) enables its multiple functions throughout the viral life cycle, making it an attractive therapeutic target [16]. The essential functions of both NP and VP40 render them suitable therapeutic targets, as VP40 inhibition would potentially prevent VLP formation and viral egress from infected cells, thereby limiting viral spread, while NP blockade would disrupt RNA encapsidation and impede the recruitment of other virion proteins [16,17].

Several studies have investigated natural product-derived therapeutic agents against EBOV to expand the limited armamentarium against this disease [18,19]. Computational approaches have been increasingly employed, given the paucity of small-molecule therapies against EBOV and the biosafety level 4 (BSL-4) containment required for experimental work with live virus [20,21]. However, most computational studies have focused on single target proteins (e.g., VP40, VP35, or NP individually) [20-22], which limits insights into multi-target therapeutic approaches that might offer enhanced efficacy and reduced resistance potential. Consequently, the simultaneous dual-inhibitory potential of individual small-molecule therapeutic agents remains largely unexplored.

Glycyrrhiza glabra (licorice), a well-known medicinal plant in traditional medicine systems, has demonstrated diverse pharmacological properties, including antiviral, anti-inflammatory, and immunomodulatory effects [23,24]. The plant's phytochemical repertoire includes flavonoids, saponins, and chalcones with documented bioactivities against various viruses [25,26]. Two reference compounds, Laurifolin (CID: 44257868) and Licochalcone A (CID: 5318998), were selected as control drugs in this *in-silico* investigation due to their reported antiviral, anti-inflammatory, and anticancer activities. Notably, Licochalcone A, a bioactive constituent of *Glycyrrhiza inflata*, has

previously demonstrated inhibitory potential against the EBOV nucleoprotein in computational studies [21,27]. In addition to its antiviral properties, Licochalcone A exhibits well-documented anti-inflammatory, antimalarial, and anticancer effects [28,29]. On the other hand, Laurifolin, an active phytoconstituent of *Rollinia laurifolia*, has also been reported to exhibit antiviral and anti-inflammatory activities, along with notable antioxidant potential [30]. However, no comprehensive investigation has simultaneously evaluated *G. glabra* phytochemicals against both VP40 and NP targets. To address this research gap, we selected two critical therapeutic targets such as VP40 and NP based on their essential roles in EBOV pathogenesis. We employed a comprehensive *in-silico* approaches to identify phytochemicals from *G. glabra* with potential dual-inhibitory effects against both target proteins. In this study, phytochemicals derived from *G. glabra* were initially screened using a virtual screening approach, and their binding affinities were evaluated in comparison with selected control compounds. The shortlisted molecules were subsequently assessed for drug-likeness and ADMET (absorption, distribution, metabolism, excretion, and toxicity) properties, leading to the exclusion of candidates with unfavourable pharmacokinetic profiles or potential toxicological risks. The most promising protein–ligand complexes were further investigated through molecular dynamics simulations and MM-PBSA (Molecular Mechanics Poisson-Boltzmann Surface Area) calculations to assess binding stability and interaction dynamics. Finally, we screened two promising compounds, Semilicoisoflavone B and Licoisoflavone B, with dual inhibitory properties against the VP40 and NP of the EBOV. Although our study employs comprehensive computational approaches that cannot fully recapitulate the dynamic complexity of biological systems, the findings provide a rational foundation for subsequent *in-vitro* and *in-vivo* experimental validation to substantiate the predicted antiviral potential of these identified phytochemicals.

Results

Virtual screening and molecular docking of the *G. glabra*-derived compounds

Virtual screening was employed to prioritize phytochemicals from *G. glabra*. A total of 408 phytocompounds were retrieved from the IMPPAT 2.0 database. Following safety screening based on bioactivity data and hazard classifications from PubChem database, 69 compounds were retained. These compounds were docked against VP40 (PDB ID: 4LDB) and nucleoprotein (NP, PDB ID: 4Z9P), showing binding affinities ranging from −11.0 to −4.8 kcal/mol and −9.2 to 3.9 kcal/mol, respectively. Candidates with higher binding affinity than control ligands Licochalcone A for NP (−7.3 kcal/mol) and Laurifolin for VP40 (−8.8 kcal/mol) were selected. Ultimately, 34 compounds were selected for further investigation due to their greater binding affinity relative to two control ligands (**Table 1** and **Table S1**).

Drug-likeness and pharmacokinetic properties of the *G. glabra*-derived compounds

The selected 34 compounds were evaluated for key molecular properties, including molecular weight and the number of rotatable bonds (NRBs), as well as hydrogen-bonding parameters such as hydrogen bond acceptors (HBAs) and hydrogen bond donors (HBDs). Lipophilicity and polarity-related parameters, including lipophilicity (LogP), topological polar surface area (TPSA), and molar refractivity (MR) as electronic descriptors, together with the bioavailability score (BS), were also assessed. Most compounds complied with Lipinski's Rule of Five, with three exceptions. Two compounds violated Veber rules, and seven violated Egan rules, primarily due to TPSA values. Compounds complying with all three rulesets (Lipinski, Veber, Egan) were selected for further evaluation. Finally, 29 compounds demonstrated drug-like potential (**Table S2**). Key absorption parameters, including water solubility and human intestinal absorption (HIA), were evaluated. Among the 29 selected compounds, Semilicoisoflavone B (CID: 5481948) and

Licoisoflavone B (CID: 5481234) demonstrated the most favorable overall ADMET profiles and were ranked as the most promising inhibitors in the dataset (**Table S3**). The water solubility values of these two compounds were −3.485 and −3.544, respectively. This trend was also reflected in their HIA, where both compounds exceeded 90%; Semilicoisoflavone B showed a notably high value of 98.022%, while Licoisoflavone B exhibited 90.761%, indicating favorable solubility under physiological conditions. The distribution profile was assessed based on the human volume of distribution (Vdss), where values below −0.15 indicated low distribution and those above 0.45 indicated high distribution. Both compounds demonstrated Vdss values above this threshold, measuring 0.486 for Semilicoisoflavone B and 0.505 for Licoisoflavone B (**Table S3**). Regarding metabolism, neither compound acted as an inhibitor of the key isoenzymes CYP3A4 and CYP2D6; however, Semilicoisoflavone B was identified as a substrate of CYP3A4. Major toxicological endpoints, including hepatotoxicity, neurotoxicity, cardiotoxicity, mutagenicity, carcinogenicity, and cytotoxicity, were evaluated, and both compounds were found to be non-toxic across all parameters, consistent with their favorable safety profiles (**Table 2**). Furthermore, both Semilicoisoflavone B and Licoisoflavone B were inactive in the AMES test and did not inhibit hERG I or hERG II. The predicted oral rat acute toxicity (LD_{50}) values were within an acceptable range, with values of 2.404 for Semilicoisoflavone B and 2.397 for Licoisoflavone B, and neither compound exhibited skin sensitization. According to pkCSM predictions, the maximum tolerated doses were 0.488 log mg/kg/day for Semilicoisoflavone B and 0.502 log mg/kg/day for Licoisoflavone B, indicating moderate tolerability without a narrow therapeutic window and supporting flexibility in early-stage dose optimization.

Binding affinities of the *G. glabra*-derived compounds with target proteins

The protein-ligand interactions, including key contact residues and two-dimensional interaction diagrams of the lead compounds with VP40 and the NP are shown **Figs. 1A-D**. Both Licoisoflavone B and Semilicoisoflavone B exhibited higher binding affinities than controls (Licochalcone and Laurifolin). For VP40, Licoisoflavone B displayed the highest binding affinity of −10.6 kcal/mol by forming several hydrogen bonds with key residues GLN155, ARG214, LEU98, and GLY99 with a bond distance ranging from 2.198 to 3.531 Å **(Table S4)**. Correspondingly, Semilicoisoflavone B formed a total of six hydrogen bonds with highly favorable bond distances. These interactions involved residues GLN155, ARG214, HIS315, and ALA156, with most bond lengths falling within 2 Å, suggesting stable and favorable binding to the target protein. It also established additional interactions at residues comparable to those observed for Licoisoflavone B. In contrast, the control compound Laurifolin formed only three conventional hydrogen bonds with residues LEU288 and ARG151, along with weaker alkyl and π-alkyl interactions (**Table S5**). The screened compounds demonstrated strong binding affinity toward the second major target, NP, exceeding that of the reference control Licochalcone A (−7.3 kcal/mol). The lead compound Licoisoflavone B exhibited the highest binding affinity (−9.7 kcal/mol) and formed three conventional hydrogen bonds with residues ASN207, ASN207, and ASP71, with bond distances of 1.82726, 2.55351, and 2.47543 Å, respectively (**Table S5**). In addition, it established three alkyl and π-alkyl interactions with the target protein. Similarly, Semilicoisoflavone B showed a strong binding affinity (−9.2 kcal/mol) and formed multiple stable hydrogen bonds involving residues PHE66, ASN207, and ASP71. In contrast, the control compound formed fewer stable hydrogen bonds, interacting with residues PHE66 and VAL199 at bond distances of 2.15059 Å and 1.85115 Å, respectively.

Dynamics simulation reveals stable interactions of the *G. glabra*-derived compounds with target proteins

To quantitatively assess the stability and compactness of the simulated complexes, the mean values of RMSD, RMSF, radius of gyration (Rg), SASA, hydrogen bonding, and MoLSA were evaluated throughout the 100 ns simulations (**Table 3**). For VP40–ligand complexes, RMSD profiles indicated overall structural stability (**Fig. 2A**), with the VP40–Licoisoflavone B complex showing the highest stability (mean RMSD 2.23 Å; STDEV 0.26 Å), reaching convergence after 40 ns. The VP40–Semilicoisoflavone B system exhibited slightly higher deviations (mean 2.43 Å; STDEV 0.39 Å) and increased fluctuations in the final 20 ns (**Fig. 2A**). In NP–ligand complexes, rapid equilibration occurred within 20 ns (**Fig. 2B**). The NP–Licoisoflavone B complex showed moderate stability (mean RMSD 2.28 Å; STDEV 0.46 Å), despite transient fluctuations between 80–95 ns, while the NP–Semilicoisoflavone B system displayed a more consistent trajectory (mean 2.33 Å; STDEV 0.33 Å), comparable to the control (**Fig. 2B**). Additional RMSD analysis (**Figs. 2C** and **2D**) revealed that Semilicoisoflavone B maintained stable binding with VP40 (mean 2.80 Å; STDEV 0.58), whereas Licoisoflavone B showed moderate compatibility (mean 3.69 Å). The control ligand exhibited increasing instability, reaching a maximum deviation of 12.66 Å (**Fig. 2C**). For NP–ligand complexes, Semilicoisoflavone B sustained stable equilibrium (mean 3.22 ± 0.90 Å), outperforming the control, while Licoisoflavone B showed significant instability, with a conformational shift around 50 ns leading to a peak RMSD of 16.77 Å and a higher average deviation (8.47 Å) (**Fig. 2D**).

To evaluate ligand-induced effects on internal dynamics and local conformational stability, C-alpha RMSF was calculated over the 100 ns trajectories (**Figs. 2E** and **2F**). The VP40–ligand complexes showed reduced flexibility, with a lower global mean RMSF for the Licoisoflavone B

system (1.39 Å) than the control (1.56 Å). Licoisoflavone B effectively suppressed fluctuations in loop regions (residues 275–285) and the C-terminal segment, indicating enhanced stabilization. In contrast, the Semilicoisoflavone B complex exhibited elevated mobility in solvent-exposed loops (maximum 6.61 Å at Lys279), suggesting weaker structural complementarity (**Fig. 2E**). For NP–ligand complexes, the core scaffold remained largely stable, with most residues fluctuating below 2.0 Å. However, increased flexibility was observed in the N-terminal domain (residues 35–45), where Semilicoisoflavone B showed a prominent peak at Ala35 (10.94 Å), exceeding that of Licoisoflavone B (8.04 Å) and the control (6.76 Å). The higher global mean RMSF (1.90 Å) further indicates ligand-induced enhancement of backbone plasticity (**Fig. 2F**).

The Rg was analyzed to assess structural integrity and folding stability of the protein–ligand systems over the 100 ns simulation (**Figs. 3A** and **3B**). Among the VP40–ligand complexes, Licoisoflavone B showed the highest compactness (19.41 ± 0.19 Å), slightly lower than the reference Leurofoline (19.52 ± 0.15 Å). In contrast, Semilicoisoflavone B exhibited a marginally higher mean Rg (19.82 ± 0.19 Å) while remaining stable throughout the simulation (**Fig. 3A**). For the NP–ligand complexes, all systems demonstrated highly stable folding behavior. Licoisoflavone B and Semilicoisoflavone B showed mean Rg values of 21.95 ± 0.17 Å and 21.98 ± 0.16 Å, respectively, indicating slightly greater compactness relative to the control ligand, Licochalcone A (22.01 ± 0.17 Å) (**Fig. 3B**). To assess ligand-induced effects on tertiary structure and conformational stability, SASA was monitored throughout the simulation (**Fig. S1A-B**). In VP40 complexes, overall SASA values were lower than in NP, reflecting intrinsic structural differences. Licoisoflavone B showed the greatest reduction in solvent exposure (12450.66 ± 239.94 $Å^2$), with a noticeable dip between 50–60 ns, indicating increased compactness. In contrast, the control (Leurofoline) maintained the highest mean SASA (12745.16 ± 212.55 $Å^2$) (**Fig. S1A**). A similar

pattern was observed for NP complexes, where SASA remained highly stable across all systems. Licoisoflavone B again exhibited the lowest mean SASA (14270.45 ± 228.99 Å²), compared with Semilicoisoflavone B (14322.24 ± 295.66 Å²) and the control Licochalcone A (14353.32 ± 282.47 Å²), suggesting a relatively more rigid and compact protein–ligand assembly (**Fig. S1B**). The stability of the protein–ligand complexes was further assessed via intermolecular hydrogen bond analysis (**Figs. 3C** and **3D**). In VP40 complexes, hydrogen bond counts were lower but steady throughout the 100 ns simulation. VP40–Semilicoisoflavone B displayed exceptional stability (mean 436.68; SD 11.13; range 409–468). VP40–Licoisoflavone B (mean 437.05) and the control VP40–Leurofoline (mean 440.18) followed nearly identical trajectories, with early convergence and maintenance of equilibrium over the full simulation period (**Fig. 3C**). Similarly, in NP complexes, hydrogen bonding remained frequent and stable, with NP–Semilicoisoflavone B showing the strongest profile (mean 514.92; range 474–554), indicating firm anchoring within the active site. The control, NP–Licochalcone A, exhibited a similar trend (mean 511.92), while NP–Licoisoflavone B was slightly less consistent (mean 505.37; SD 13.34) (**Fig. 3D**). Intra-molecular hydrogen bonds were tracked over the 100 ns simulation to assess structural integrity and conformational stability (**Fig. S1C** and **D**). In VP40 complexes, all systems exhibited strong internal connectivity. The control, VP40–Leurofoline, had the highest mean H-bonds (6.82 ± 1.39), while VP40–Semilicoisoflavone B and VP40–Licoisoflavone B showed comparable stability (5.98 ± 1.14 and 5.82 ± 1.23, respectively). The low SD and consistent min–max values indicate persistent interactions and well-equilibrated structures (**Fig. S1C**). For NP complexes, test ligands formed more extensive H-bond networks than the control. NP–Semilicoisoflavone B and NP–Licoisoflavone B maintained robust internal stabilization (6.07 ± 1.18 and 5.98 ± 1.34), whereas the control NP–Licochalcone A exhibited a significantly lower mean of 3.18 ± 1.05. The higher

intra-molecular H-bond frequency in the test compounds likely contributes to enhanced internal stability and lower RMSD values observed in these complexes (**Fig. S1D**). MolSA was analyzed to evaluate the effect of ligand binding on protein compactness and folding integrity (**Figs. S2A** and **B**). In VP40 complexes, high structural conservation was observed, with mean MolSA values of 12820.90 Å² for Licoisoflavone B, 12926.93 Å² for Semilicoisoflavone B, and 12929.63 Å² for the control (Leurofoline) (**Fig. S2A**). For NP complexes, MolSA remained consistent across all systems. Licoisoflavone B showed a mean of 14318.03 Å² (min 13624.76, max 15033.94; SD 250.39), slightly more compact than the control (SD 262.20), suggesting enhanced structural rigidity. Semilicoisoflavone B (mean 14475.65 Å²) closely matched the control (14477.43 Å²), reflecting maintenance of a native-like surface environment (**Fig. S2B**). Van der Waals surface area (VSA) was analyzed to assess structural compactness and ligand-induced effects on protein topology (**Figs. S2C** and **D**). In VP40 complexes, structural conservation was maintained, with mean VSA values of 23379.13 Å² for Licoisoflavone B, 23395.04 Å² for Semilicoisoflavone B, and 23455.92 Å² for the control (Leurofoline) (**Fig. S2C**). For NP complexes, VSA remained stable within a narrow range (≈27,141–28,213 Å²). Mean VSA values were 27540.36 ± 151.78 Å² for Licoisoflavone B, 27571.70 ± 145.49 Å² for Semilicoisoflavone B, and 27602.15 ± 147.32 Å² for the control (Licochalcone A). The low SDs indicate that the proteins retained stable, globular conformations, with Licoisoflavone B showing a slightly more compact assembly relative to the control (**Fig. S2D**).

MM-PBSA binding free energy reveals stable interactions of the *G. glabra*-derived compounds with target proteins

To quantify the binding affinity and thermodynamic stability of the selected ligands within the catalytic pockets of VP40 and NP of EBOV, MM-PBSA (Molecular Mechanics Poisson–

Boltzmann Surface Area) calculations were performed over the stable 100 ns trajectory (**Figs. S3A and B)**. The binding free energy (ΔG_{bind}) provided a comprehensive measure of interaction strength, with more negative values indicating higher affinity between the protein and ligand. The binding landscape of the VP40 protein revealed a more stabilized interaction profile. The control ligand, Leurofoline, demonstrated the highest affinity, with an average ΔG_{bind} of −152.46 kcal/mol. Among the test compounds, Semilicoisoflavone B showed strong performance, with an average binding energy of −129.21 kcal/mol and a minimum value of −253.46 kcal/mol, suggesting maintenance of a highly favorable orientation within the binding site. In contrast, Licoisoflavone B exhibited comparatively lower affinity for VP40 (−42.32 kcal/mol) (**Fig. S3A**). on the other hand, both Licoisoflavone B and Semilicoisoflavone B exhibited stronger binding profiles than the reference control, Licochalcone A. The average ΔG_{bind} values for Licoisoflavone B and Semilicoisoflavone B were −35.42 kcal/mol and −35.74 kcal/mol, respectively, whereas the control showed a negligible average binding energy of −0.20 kcal/mol. Despite these favorable averages, high standard deviations (53.48 and 69.23 kcal/mol) were observed, suggesting notable conformational fluctuations during the simulation. This observation was supported by trajectory analysis, which revealed transient peak binding energies as low as −234.19 kcal/mol for Licoisoflavone B, indicating periods of strong molecular recognition followed by equilibration (**Fig. S3B**).

Principal component analysis reveals stable conformational landscape between *G. glabra*-derived compounds with target proteins

Principal component analysis (PCA) was conducted to investigate the conformational landscapes and collective motions of the target proteins (VP40 and NP)-ligand complexes (**Figs. S4A-C** and **Figs. S5A-C**). For VP40 complexes**,** VP40–Semilicoisoflavone B exhibited the highest total

eigenvalue (971.10), reflecting broader conformational sampling and greater structural flexibility. On the contrary, VP40–Licoisoflavone B and the control VP40–Leurofoline showed lower total eigenvalues of 439.47 and 586.43, respectively, indicating more constrained and stable global motions. Variance analysis across the first three principal components (PC1–PC3) captured most essential dynamics. VP40–Licoisoflavone B was dominated by PC1, which accounted for 64.21% of the total variance (Mean: −130.003; SD: 16.636; Max: −104.687), suggesting that the system's motion was governed primarily by a single mode (**Fig. S4A**). Conversely, VP40–Semilicoisoflavone B and the control exhibited a more distributed variance: for Semilicoisoflavone B, PC1 contributed 53.81% (Mean: −78.345; SD: 22.993; Max: −36.907), with PC2 and PC3 contributing 32.61% and 13.57%, respectively (**Fig. S4B**). The control drug Leurofoline displayed a similar distribution, with PC1 variance of 52.05% (Mean: 22.041; SD: 22.594; Max: 76.586) (**Fig. S4C**). For NP complexes, NP–Licoisoflavone B showed moderate conformational mobility, with a total eigenvalue of 968.78. PC1, PC2, and PC3 accounted for 44.59%, 31.10%, and 24.31% of the total variance, respectively (PC1 range: −82.5411 to 26.77431; Mean: −27.3721; SD: 20.811) (**Fig. S5A**). Conversely, NP–Semilicoisoflavone B displayed the highest structural variation, with a total eigenvalue of 1705.18. PC1 dominated the motion, capturing 62.94% of variance (Mean: −5.987; SD: 32.889; Max: 49.875; Min: −68.791), while PC2 and PC3 contributed 24.21% and 12.85%, indicating movement concentrated along a primary directional mode (**Fig. S5B**). The control, NP–Licochalcone A, had the lowest total eigenvalue (856.02), suggesting a more restricted conformational space and enhanced stability. PC1 accounted for 40.59% of variance (range: −131.921 to −36.184; Mean: −85.217; SD: 18.623), with lower standard deviations across primary components, reflecting relatively rigid structural behavior during the simulation (**Fig. S5C**). This PCA analysis highlights how ligand binding modulates

global motions and conformational flexibility, with Semilicoisoflavone B generally promoting higher mobility and Licoisoflavone B producing more constrained dynamics in both VP40 and NP systems.

Quantum mechanics analysis reveals thermodynamic stability and electronic characteristics of *G. glabra*-derived compounds

Density Functional Theory (DFT) calculations were conducted to evaluate the intrinsic electronic properties of the three lead compounds and the reference ligands. Key parameters, including molecular weight (g/mol), electronic energy, enthalpy, Gibbs free energy, dipole moment, and entropy, are summarized in **Table S6**. Both Semilicoisoflavone B and Licoisoflavone B exhibited more negative electronic energy values (−1223.079 Hartree and −1223.087 Hartree, respectively), indicating enhanced electronic stability. Semilicoisoflavone B displayed the most negative Gibbs free energy (−1223.153 Hartree), suggesting the highest thermodynamic stability under standard conditions. Licoisoflavone B demonstrated a higher dipole moment (5.378 Debye) than Semilicoisoflavone B (4.459 Debye), and both compounds showed greater polarity compared to the reference ligands (**Table S6**). The molecular electrostatic potential (MEP) surfaces of the two lead compounds and the reference ligands were analyzed using geometry-optimized structures. In the MEP maps, red regions corresponded to electron-rich (negative) potential, while blue and green regions represented electron-deficient (positive) or neutral zones (**Fig. 4**). For all compounds, negative electrostatic potentials were primarily localized around oxygen atoms, whereas positive potentials were distributed near hydrogen atoms. The range of positive electrostatic potential extended from 7.285×10^{-2} eV to 8.193×10^{-2} eV. Both lead compounds exhibited similar distributions of positive and negative potentials, with Licoisoflavone B showing slightly higher magnitudes (-7.793×10^{-2} eV and 7.793×10^{-2} eV) compared to Semilicoisoflavone B ($-7.504 \times$

10^{-2} eV and 7.504×10^{-2} eV). In contrast, the control ligands (Licochalcone A and Laurifolin) displayed the lowest and highest positive potentials, at 7.285×10^{-2} eV and 8.193×10^{-2} eV, respectively (**Fig. 4**).

The HOMO–LUMO energy gaps of the studied compounds, Semilicoisoflavone B and Licoisoflavone B, were calculated to be 4.21 eV and 3.69 eV, respectively, while the reference ligands, Leurofoline and Licochalcone A, exhibited energy gaps of 4.41 eV and 4.07 eV (**Fig. 5** and **Table S6**). Licoisoflavone B showed the lowest energy gap among all compounds, suggesting enhanced chemical stability and greater molecular polarizability, although its reduced kinetic stability reflects the relative ease of electronic transitions. These observations were further supported by global hardness (η) and chemical softness analyses, where Licoisoflavone B displayed the lowest hardness and highest softness values compared to Semilicoisoflavone B and the reference ligands.

The electronic absorption properties of the two lead compounds and their respective control ligands were investigated at the B3LYP/6-311++G(d,p) level of theory (**Table S7** and **Fig. S6A**). Semilicoisoflavone B exhibited a maximum absorption (λ_{max}) at 384.38 nm, whereas Licoisoflavone B showed a pronounced red shift with λ_{max} at 534 nm with a slightly higher oscillatory strength (f = 0.006). In comparison, the reference compound at 285.60 nm (3.711 eV) with a greater oscillator strength (f = 0.041), whereas Licochalcone A displayed absorption at 496.31 nm (2.066 eV) with a lower transition (f = 0.001). The substantial bathochromic shift observed in Licoisoflavone B correlates with its lowest HOMO–LUMO energy gap (3.69 eV) and the highest electrophilicity index (ω = 3.91), reflecting enhanced chemical reactivity relative to Semilicoisoflavone B (ΔE = 4.21 eV) and the control compounds. Semilicoisoflavone B exhibited moderate chemical hardness (η = 2.10) and stability. The vibrational spectra of the two lead

compounds and the control ligands were analyzed using DFT calculations with a scaling factor of 0.9688 **(Table S8** and **Fig. S6B)**. Broad O–H stretching vibrations were observed at 3658.51 cm^{-1} for Semilicoisoflavone B, 3214.10 cm^{-1} for Licoisoflavone B, 3243.51 cm^{-1} for Leurofoline, and 3712.12 cm^{-1} for Licochalcone A. Aliphatic and aromatic C–H stretching modes appeared within the 2915–2943 cm^{-1} range, while strong carbonyl (C=O) stretching vibrations were detected at 1659.21, 1615.83, 1625.82, and 1629.15 cm^{-1}, respectively. Aromatic C=C stretching vibrations were identified in the 1555–1616 cm^{-1} region, indicating extended π-conjugation across the aromatic rings.

Discussion

The identification of effective small-molecule inhibitors against EBOV remains a critical global health priority, particularly given the logistical challenges associated with monoclonal antibody therapies in resource-limited settings [11,18,21]. In this context, the present study identified two lead compounds, Semilicoisoflavone B and Licoisoflavone B, derived from *G. glabra*, as promising dual-target inhibitors of the VP40 matrix protein and NP of the EBOV [13,15]. By simultaneously targeting two essential structural proteins, these compounds offer a multifaceted therapeutic strategy that may reduce the risk of viral resistance development. To evaluate these interactions, molecular docking, a widely employed technique in structure-based drug discovery, enables atomic-level evaluation of protein-ligand interactions [21,31]. Notably, both lead compounds demonstrated superior binding affinities against VP40 and NP compared to their respective control ligands (Laurifolin and Licochalcone A), with binding scores ranging from -9.2 to -10.6 kcal/mol. These values suggest stable complex formation and enhanced target specificity, consistent with previously reported EBOV inhibitors [32,33]. Following docking analysis, drug-likeness assessment revealed that both Semilicoisoflavone B and Licoisoflavone B satisfied Lipinski's Rule of Five,

Veber, and Egan criteria, indicating favorable oral bioavailability potential [32,34]. Furthermore, pharmacokinetic profiling further supported their developmental suitability, with excellent predicted human intestinal absorption (>90%), moderate volume of distribution, and minimal blood-brain barrier penetration, thereby reducing central nervous system-related toxicity risks [35]. Additionally, neither compound inhibited CYP3A4 or CYP2D6, suggesting a reduced tendency for metabolic drug-drug interactions [36]. Toxicity predictions indicated non-mutagenic, non-carcinogenic, and non-cardiotoxic profiles, with no hERG I/II inhibition, a critical safety feature given the association between hERG blockade and drug-induced arrhythmias [37]. Regarding binding modes, detailed interaction analysis revealed that Licoisoflavone B formed multiple hydrogen bonds with key VP40 residues (GLN155, ARG214, LEU98, GLY99), while Semilicoisoflavone B established stable hydrogen bonds with GLN155, ARG214, HIS315, and ALA156, with bond distances below 2 Å indicative of strong interactions [38]. For NP, both compounds engaged critical residues including ASN207, ASP71, and PHE66 through hydrogen bonding and hydrophobic contacts. Such multi-modal interactions, encompassing hydrogen bonds, π-cation, and π-π stacking, contribute to enhanced binding stabilization within viral protein targets [34,39].

To assess dynamic behavior, MDSs over 100 ns confirmed the structural integrity of protein-ligand complexes. The VP40-Licoisoflavone B complex exhibited exceptional stability with a mean RMSD of 2.23 Å and low standard deviation (0.26 Å), while NP-Semilicoisoflavone B maintained consistent RMSD values (2.33 ± 0.33 Å), indicating robust binding [40]. Moreover, ligand RMSD analysis showed that Semilicoisoflavone B retained positional stability within both targets, whereas Licoisoflavone B displayed target-dependent behavior—greater stability with VP40 but conformational adjustments within NP, reflecting dynamic adaptation to different binding

environments [41]. Consequently, RMSF analysis revealed that most residues fluctuated below 2.0 Å, with Licoisoflavone B effectively suppressing loop region mobility (residues 275–285) in VP40, suggesting enhanced stabilization [42]. Furthermore, Rg and SASA analyses confirmed that all complexes maintained compact, folded conformations throughout simulations, with no evidence of structural expansion or unfolding [43,44]. Additionally, intermolecular hydrogen bond analysis demonstrated sustained interactions, particularly for NP-Semilicoisoflavone B (mean 514.92 bonds), corroborating stable binding. Intramolecular hydrogen bond networks were also well-preserved, with test compounds showing superior internal stabilization compared to controls [42,45]. To quantify binding strength, MM-PBSA binding free energy calculations quantified the thermodynamic favorability of interactions. Semilicoisoflavone B exhibited exceptional affinity for VP40 (ΔG = -129.21 kcal/mol), while both compounds showed favorable binding to NP ($\Delta G \approx$ -35.5 kcal/mol), outperforming the NP control ligand (ΔG = -0.20 kcal/mol). These values underscore the robust interaction strengths and potential antiviral efficacy [41]. In terms of conformational dynamics, PCA revealed that Licoisoflavone B constrained conformational space (total eigenvalue 439.47 for VP40), indicating reduced flexibility and enhanced stability, whereas Semilicoisoflavone B exhibited broader essential dynamics, reflecting adaptive binding capabilities [46].

At the electronic level, DFT calculations provided insights into electronic properties governing molecular reactivity. Licoisoflavone B exhibited the smallest HOMO-LUMO energy gap (3.69 eV) among studied compounds, indicating higher chemical reactivity and polarizability, facilitating stronger interactions with biological macromolecules [47]. This was consistent with its higher electrophilicity index (ω = 3.91) and chemical softness. Moreover, both lead compounds demonstrated favorable thermodynamic stability, with highly negative electronic energies (-

1223.079 to -1223.087 Hartree) and Gibbs free energies. Additionally, MEP maps localized electron-rich regions around oxygen atoms, identifying potential nucleophilic sites for electrostatic interactions with positively charged amino acid residues (e.g., arginine, lysine) within binding pockets [48]. Furthermore, the TD-DFT UV–visible spectral analysis revealed significant electronic transitions in the compounds under investigation. Licoisoflavone B showed a considerable bathochromic shift (λ_{max} = 534 nm), suggesting improved π electron delocalization and charge-transfer potential throughout its molecular framework. This characteristic aligns well with its reduced HOMO-LUMO energy gap and elevated electrophilicity index, thereby implying increased chemical reactivity. Conversely, Semilicoisoflavone B (λ_{max} = 384.38 nm) exhibited more balanced electronic properties. Furthermore, FT-IR vibrational analysis confirmed key functional groups including hydroxyl, carbonyl, and aromatic C=C bonds—that contribute to hydrogen bonding and π-stacking interactions with protein residues, further supporting stable complex formation [49].

Nevertheless, despite comprehensive *in-silico* analyses, this study has several limitations. Computational predictions cannot fully replicate dynamic biological systems, and the absence of *in-vitro* and *in-vivo* validation restricts conclusive therapeutic claims. Specifically, the proposed dual-target mechanism, involving the simultaneous inhibition of both VP40 and NP, required experimental validation through binding assays and cellular models to confirm concurrent target engagement. Therefore, future research should focus on experimental validation including surface plasmon resonance studies, antiviral activity assays in EBOV-infected cell lines, and subsequent animal model evaluations to establish clinical potential.

Conclusion

This study applied an integrated *in-silico* computational approach to evaluate bioactive phytocompounds from *G. glabra* as promising dual inhibitors of the Ebola virus VP40 matrix protein and NP. Molecular docking, 100 ns MDSs, PCA, MM-PBSA, and density functional theory–based quantum mechanical analyses were employed to identify ligands capable of stable binding to both targets. Two phytocompounds, namely Semilicoisoflavone B and Licoisoflavone B, exhibited stronger binding affinities than the reference ligands Laurifolin and Licochalcone A. Notably, both compounds showed particularly favorable interaction patterns, marked by persistent hydrogen bonding and hydrophobic contacts with key residues including GLN155, ARG214, LEU98, and GLY99 (VP40) and ASN207, ASP71, and PHE66 (NP). Interaction stability over the 100 ns simulation trajectories was supported by RMSD, RMSF, Rg, and MM-PBSA analyses, indicating sustained and energetically favorable binding conformations. ADMET predictions further suggested acceptable pharmacokinetic profiles, with both compounds complying with Lipinski's Rule of Five, showing favorable intestinal absorption, and lacking predicted hepatotoxicity, cardiotoxicity, or mutagenicity. Thus, these results highlight Semilicoisoflavone B and Licoisoflavone B as promising lead candidates for dual-target inhibition of EBOV.

Methods

Ethical statement

This study was conducted entirely using *in-silico* computational approaches, including molecular docking and virtual screening. As the research did not involve human participants, personal data, animal experimentation, or biological sample collection, institutional ethical approval was not

required. The authors confirm that the study complies with the publication ethics and responsible research standards established by Scientific Reports.

Protein structure preparation

The three-dimensional crystal structures for two Ebola virus proteins were obtained from the RCSB Protein Data Bank. The matrix protein VP40 was obtained from the entry with PDB ID 4LDB, which features a resolution of 3.10 Å and an R-free value of 0.28 [16]. Likewise, the core domain of the viral nucleoprotein (NP; PDB ID: 4Z9P) was obtained from the higher-resolution structure (1.79 Å, R-free: 0.225) [14]. To prepare these structures for subsequent computational analysis, a standardized refinement protocol was implemented using BIOVIA Discovery Studio 2024 [39]. This preparation involved isolating the single chain of interest by extracting Chain A from each structure and removing the remaining components, including additional chains, water molecules, bound ligands, and other heteroatoms. The cleaned monomeric structures were then energy-minimized using the GROMOS96 force field in SWISS-PDB Viewer [50] to optimize atomic contacts, relieve steric strain, and stabilize the overall protein conformation. The overall workflow is outlined in **Fig. S1**, providing a schematic representation of the methodology employed in this study.

Retrieval and preparation of *G. glabra*-derived compounds

Phytocompounds from *G. glabra* were sourced from the curated database Indian Medicinal Plants, Phytochemistry And Therapeutics 2.0 (IMPPAT 2.0), which currently catalogues 4,010 medicinal plants, 17,967 phytochemicals, and 1,095 therapeutic uses, and related data [34,51]. A total of 408 bioactive compounds from five medicinal plant species including *G. glabra* were retrieved from the IMPPAT 2.0 database [52]. To ensure a rigorous and unbiased selection process, a multi-step screening strategy was employed. The compounds were initially selected based on documented bioactivity data for antiviral or related therapeutic effects, as curated from the IMPPAT 2.0

database. To ensure laboratory and clinical safety, each compound was screened against its hazard classifications in the PubChem database [53]. Following a primary filter to exclude compounds with major hazard classifications (e.g., irritant, highly flammable, serious health hazard), a refined set of 69 compounds with promising safety profiles was retained for downstream analysis.

Prior to the docking analysis, the compounds were obtained in Structure-Data File (SDF) format with three-dimensional conformations from the PubChem database [53]. Prior to the docking analysis, each of the phytocompounds was screened through MarvinSketch (v20.8) software [54] to identify any structural discrepancies. Subsequently, the compounds were converted into PDB file format using Avogadro (v. 1.99.0) [55]. Using Python Prescription (PyRx) [15], the ligand structures were converted into PDBQT format for molecular docking. This conversion employed the Universal Force Field (UFF) within the Open Babel interface of PyRx to optimize geometries and minimize conformational energies [56]. The resulting ligand library was then utilized for subsequent virtual screening and molecular docking analyses.

Molecular docking and interaction calculation of the *G. glabra*-derived compounds

To elucidate the inhibitory effects of the selected phytocompounds against VP40 (PDB ID: 4LDB) and nucleoprotein (NP, PDB ID: 4Z9P) of the Ebola virus, PyRx software integrated with AutoDock Vina v1.2.0 platform was utilized for molecular docking [57]. Screened phytocompounds were denoted as the ligands and the proteins as macromolecules. The docking was executed without selecting the active site as it is automatically identified by the software's integrated algorithm based on the protein's three-dimensional structure [58]. For the docking of all phytocompounds with VP40 and NP, the grid boxes were centered on the proteins with dimensions of 25 × 25 × 25 Å for VP40 and 30 × 30 × 30 Å for NP along the X, Y, and Z axes, respectively. For each compound, the top nine binding poses, ranked by the calculated Vina score (in kcal/mol),

were generated and saved. The resulting docked complexes were analyzed to identify compounds with the highest predicted binding affinities (i.e., the most negative Vina scores) for each protein target. Compounds exhibiting binding affinities lower than −8.8 kcal/mol for VP40 and −7.3 kcal/mol for NP were considered for further analysis, based on comparison with control ligands Laurifolin and Licochalcone A, respectively [22]. Upon completion of the docking process, both the ligands and the target proteins were saved in pdbqt format. This file format was then used to calculate and visualize the different interactions between the proteins and compounds using BIOVIA Discovery Studio Visualizer v2024 [59]. The top-scoring poses for promising compounds were exported and imported into Discovery Studio to generate and examine both two-dimensional (2D) and three-dimensional (3D) interaction diagrams. Additionally, the docking protocol was validated through a redocking analysis performed with AutoDock Vina implemented in the PyRx v1.2.0 platform [57], using the crystal structure of the EBOV VP40 and NP in complex with control ligands Laurifolin and Licochalcone A, respectively. The protein structure was prepared by removing water molecules and other non-essential heteroatoms. The co-crystallized ligand was extracted from the binding site and converted into the pdbqt format. Redocking was carried out using AutoDock Vina implemented through the PyRx v1.2.0 platform. The grid box was centered on the original ligand-binding site, with dimensions adjusted to fully cover the active pocket. Default Vina parameters were applied to maintain reproducibility and consistency with the primary docking workflow. Docking accuracy was evaluated by superimposing the redocked ligand onto its crystallographic conformation and calculating the root-mean-square deviation (RMSD) for all atoms. An RMSD value close to or below 2.0 Å was considered indicative of acceptable predictive performance [60].

Drug-likeness and pharmacokinetic properties analysis of the *G. glabra*-derived compounds

An *in-silico* computational pharmacokinetics analysis was performed to assess the temporal dynamics of absorption, distribution, metabolism, excretion, and toxicity (ADMET) of the selected phytocompounds. Following molecular docking, the top-scoring compounds were subjected to a multi-parameter drug-likeness filter to assess their potential for oral bioavailability and pharmacokinetic feasibility using the SwissADME web tool (accessed on January 15, 2025, at https://www.swissadme.ch/) [61]. The compounds were evaluated against four established rulesets: Lipinski's Rule of Five [62], Veber's rules [63], Muegge's (MOGAN) filter [64], and Egan's rules [65]. These rules evaluate critical physicochemical properties including molecular weight (<500 Da), lipophilicity (LogP ≤ 5), numbers of hydrogen bond donors (≤5) and acceptors (≤10), rotatable bonds (≤10), and topological polar surface area (TPSA <140 Å^2) [66]. Compounds complying with all three rules (Lipinski, Veber, and Egan) without any violations were selected for further evaluation.

Key ADME parameters assessed using SwissADME [61] and pkCSM [67] servers included predicted human intestinal absorption (HIA), blood-brain barrier (BBB) penetration, cytochrome P450 enzyme inhibition profiles (CYP2D6, CYP3A4), aqueous solubility (LogS), volume of distribution (Vdss), and total clearance. Toxicity predictions were carried out through the Protox III online server (accessed on January 20, 2025, at https://comptox.charite.de/protox3/) [68] and pkCSM [67], ensuring a comprehensive evaluation of the ligands' safety profiles. The Simplified Molecular Input Line Entry System (SMILES) formats of all phytocompounds were obtained from the PubChem database. Toxicity endpoints evaluated included AMES mutagenicity, hERG I and II inhibition, hepatotoxicity, neurotoxicity, cardiotoxicity, carcinogenicity, cytotoxicity, oral rat acute toxicity (LD_{50}), skin sensitization, and maximum tolerated dose in humans. Drug-likeness of the protein-ligand complexes was evaluated using Lipinski's Rule of Five [66], ensuring all

properties fell within the accepted thresholds. The compounds were ranked based on an integrated score that prioritized favorable ADMET properties—specifically, high predicted intestinal absorption (>90%), negligible neurotoxic risk (low BBB penetration for peripheral antiviral activity), acceptable solubility, and a low probability of metabolic inhibition or toxicity.

Geometry optimization of the *G. glabra*-derived compounds

The molecular structures of the two selected phytocompounds such as Semilicoisoflavone B (CID: 5481948) and Licoisoflavone B (CID:5481234), and the control compounds namely Laurifolin (CID:44257868) and Licochalcone A (CID:5318998) were first energy-minimized using Gabedit software [69], and subsequently subjected to gas-phase geometry optimization in Gaussian 09W (Revision D.01) [70] employing Density Functional Theory (DFT) with the B3LYP hybrid functional [71] and the 6-311G+(d,p) basis set [72]. Frequency calculations were performed at the same level of theory to confirm that the optimized structures corresponded to true energy minima (no imaginary frequencies). The optimized structures were used to calculate molecular properties including electronic energy, enthalpy, Gibbs free energy, dipole moment, and entropy.

The time-dependent (TD)-DFT was utilized to analyze the highest occupied molecular orbital (HOMO) and lowest unoccupied molecular orbital (LUMO) referring to as lead molecular orbitals. This analysis provided insight into chemical reactivity [73]. The equations (I) and (II) were employed to analyze the characteristics of molecular orbitals [32].

$$Gap\ (\Delta E) = [\varepsilon LUMO - \ \varepsilon HOMO],\ \eta = \frac{[\varepsilon LUMO - \varepsilon HOMO]}{2};\ S = \frac{1}{\eta} \quad \text{---------- (I)}$$

Where: ΔE is the energy gap; $\varepsilon LUMO$ is the lowest occupied molecular orbit; $\varepsilon HUMO$ is the highest occupied molecular orbit; η is the chemical hardness; S is the chemical softness.

$$\mu = \frac{[\varepsilon LUMO + \varepsilon HOMO]}{2};\ \chi = -\frac{[\varepsilon LUMO + \varepsilon HOMO]}{2};\ \omega = \frac{\mu^2}{2\eta} \quad \text{---------- (II)}$$

Where: μ is the chemical potential; $\varepsilon LUMO$ is the lowest occupied molecular orbit; $\varepsilon HUMO$ is the highest occupied molecular orbit; χ is the electronegativity; ω is the electrophilicity index; μ is the chemical potential; η is the chemical hardness.

Molecular electrostatic potential (MEP) surfaces were generated to visualize charge distribution across the molecules, with red regions indicating electron-rich (negative) potential and blue regions indicating electron-deficient (positive) potential [74]. The thermodynamic and molecular orbital properties of the phytocompounds were visualized using the ResultView module in GaussView v.06 [75]. Electrostatic potentials were also depicted using the Surface/Contour module in GaussView v.06, enabling a comprehensive representation of the molecular characteristics.

Stability calculation of the *G. glabra*-derived compounds through dynamics simulation

To investigate the interactions between the phytocompounds and the target proteins (VP40 and NP), the top two compounds (Semilicoisoflavone B and Licoisoflavone B) along with control compounds underwent 100 ns molecular dynamics simulations (MDS). The process commenced with energy minimization and structural optimization of the protein-ligand complexes [76]. MDSs were performed using the YASARA Structure program [77] employing the AMBER14 force field for atomic interactions [78]. Each complex was prepared by solvating in a cubic box of 80 × 80 × 80 $Å^3$ using the TIP3P water model [79], neutralized with Na^+ and Cl^- ions under physiological conditions of 298 K, pH 7.4, and 0.9% NaCl, with periodic boundary conditions applied. Energy minimization was performed via the steepest descent method, followed by simulation runs where van der Waals and short-range Coulomb interactions used an 8 Å cutoff, and long-range electrostatics were computed using the Particle Mesh Ewald (PME) method [80]. Trajectory snapshots were saved every 100 ps for subsequent analysis.

Each complex was simulated for a duration of 100 ns to evaluate the stability and dynamics of the phytocompound-protein interactions. Trajectory analyses included root mean square deviation (RMSD), root mean square fluctuation (RMSF), radius of gyration (Rg), solvent accessible surface area (SASA), molecular surface area (MolSA), van der Waals surface area (VSA), and hydrogen bond interactions for stability assessment. The mathematical formulas for calculating RMSD, RMSF, and Rg are as follows [81]:

$$\text{RMSD} = \sqrt{\frac{1}{N}\sum_{i=1}^{N}(x_i - x_i^{ref})^2} \qquad \ldots\ldots\ldots \text{(III)}$$

where N is the number of atoms, and x_i and x_i^{ref} are the coordinates of the i-th atom in the current and reference structures, respectively.

$$\text{RMSF}_i = \sqrt{\frac{1}{N}\sum_{k=1}^{N}\sum_{j=1}^{3}(P_{i,j,k} - \overline{P}_{i,j})^2} \qquad \ldots\ldots\ldots \text{(IV)}$$

where N is the number of evaluated snapshots, j runs from 1 to 3 for the x, y, and z coordinates of the position vector P, $P_{i,j,k}$ is the j-th coordinate of atom i in snapshot k, and $\overline{P}_{i,j}$ is the average over all snapshots. For residues, the RMSF is the average of the RMSFs of its constituting atoms.

$$\text{Rg} = \sqrt{\frac{\sum_{i=1}^{N} m_i \|r_i - R\|^2}{M}} \qquad \ldots\ldots\ldots \text{(V)}$$

where N is the number of atoms, m_i is the mass of atom i, r_i is its position, R is the center of mass, and $M = \sum_{i=1}^{N} m_i$ is the total mass.

Quantification of the surface properties of the *G. glabra*-derived compounds during simulation

The surface properties such as SASA (Å²), MolSA (Å²), and VSA (Å²) of the phytocompounds were rigorously analyzed to assess their surface and structural dynamics during MDS. These parameters were calculated at regular intervals across the 100 ns trajectories, ensuring high temporal resolution for dynamic profiling using built-in functions in YASARA Structure. The processed data encompassed comprehensive temporal changes in surface properties, enabling a thorough understanding of the compounds' conformational behavior over time [34]. To enhance interpretability, the trajectory-derived data were systematically organized and subjected to graphical rendering using OriginPro 2024 [82] on a Windows platform. This approach allowed for the generation of detailed visual representations, facilitating an in-depth exploration of the phytocompounds' surface characteristics and their evolution throughout the simulation. The resulting dataset provided critical insights into the molecular interactions and stability of the phytocompounds under dynamic conditions, contributing valuable information to the analysis of their bioactivity and interaction mechanisms.

Binding free energy calculation of the *G. glabra*-derived compounds

The binding free energy of the phytocompounds in complex with the target proteins VP40 and NP was meticulously quantified using the Molecular Mechanics Poisson-Boltzmann Surface Area (MM-PBSA) methodology [83]. Following the 100 ns MDS, the conformational ensembles of both proteins and the bound phytocompounds were systematically extracted from the simulation trajectories, taking 1000 snapshots from the equilibrated phase (last 50 ns) of each simulation to ensure representative sampling of the dynamic interaction states [84]. The binding free energy (ΔG_{bind}) was calculated as an average over these snapshots using the following equations [48]:

$$\Delta G_{bind} = G_{complex} - (G_{protein} + G_{ligand}) \text{ ---------- (VI)}$$

$$\Delta G_{bind} = E_{MM} + G_{solv} - T\Delta S \text{ ---------- (VII)}$$

where E_{MM} represents the gas-phase molecular mechanics energy (sum of van der Waals and electrostatic interactions), G_{solv} is the solvation free energy (calculated as the sum of polar and non-polar contributions using the Poisson-Boltzmann and solvent-accessible surface area models, respectively), and TΔS denotes the entropic contribution.

Principal component analysis

To characterize the dominant collective motions of the protein backbone during the simulations, principal component analysis (PCA) was conducted on the Cα atoms [85]. The analysis was performed on the concatenated and aligned trajectory from the production phase of each system using the YASARA Structure program. First, the covariance matrix of atomic positional fluctuations was constructed after removing rotational and translational degrees of freedom. Diagonalization of this matrix yielded a set of eigenvectors (principal components, PCs) and corresponding eigenvalues, where each eigenvalue represents the mean square fluctuation along its respective eigenvector [46]. The first few PCs, which typically capture the most significant conformational changes (accounting for >70% of the total variance), were projected onto the trajectory to visualize the essential dynamics. The eigenvalues and their cumulative contributions were calculated to compare the conformational flexibility among different protein-ligand complexes.

UV-Vis and FT-IR spectral analysis

Time-dependent density functional theory (TD-DFT) was used to calculate electronic transitions and perform UV-Vis spectral analysis using the B3LYP/6-311G+(d,p) level of theory [86]. The first 20 singlet-singlet excitations were computed to simulate the absorption spectra. Additionally, vibrational frequency analysis was performed to simulate FT-IR spectra, applying a scaling factor of 0.9688 to correct for anharmonic effects and basis set limitations [87]. Key vibrational modes

including O-H stretching, C-H stretching (aliphatic and aromatic), carbonyl (C=O) stretching, and aromatic C=C stretching were identified and analyzed.

Statistical analysis

All numerical data from MDSs are presented as mean ± standard deviation (SD). RMSD, RMSF, SASA, Rg, and hydrogen bond analyses were performed using built-in functions in YASARA Structure. For MM-PBSA calculations, average binding energies and standard deviations were calculated from 1000 trajectory snapshots. PCA eigenvalues and variance contributions were computed using the covariance matrix diagonalization method.

Figures

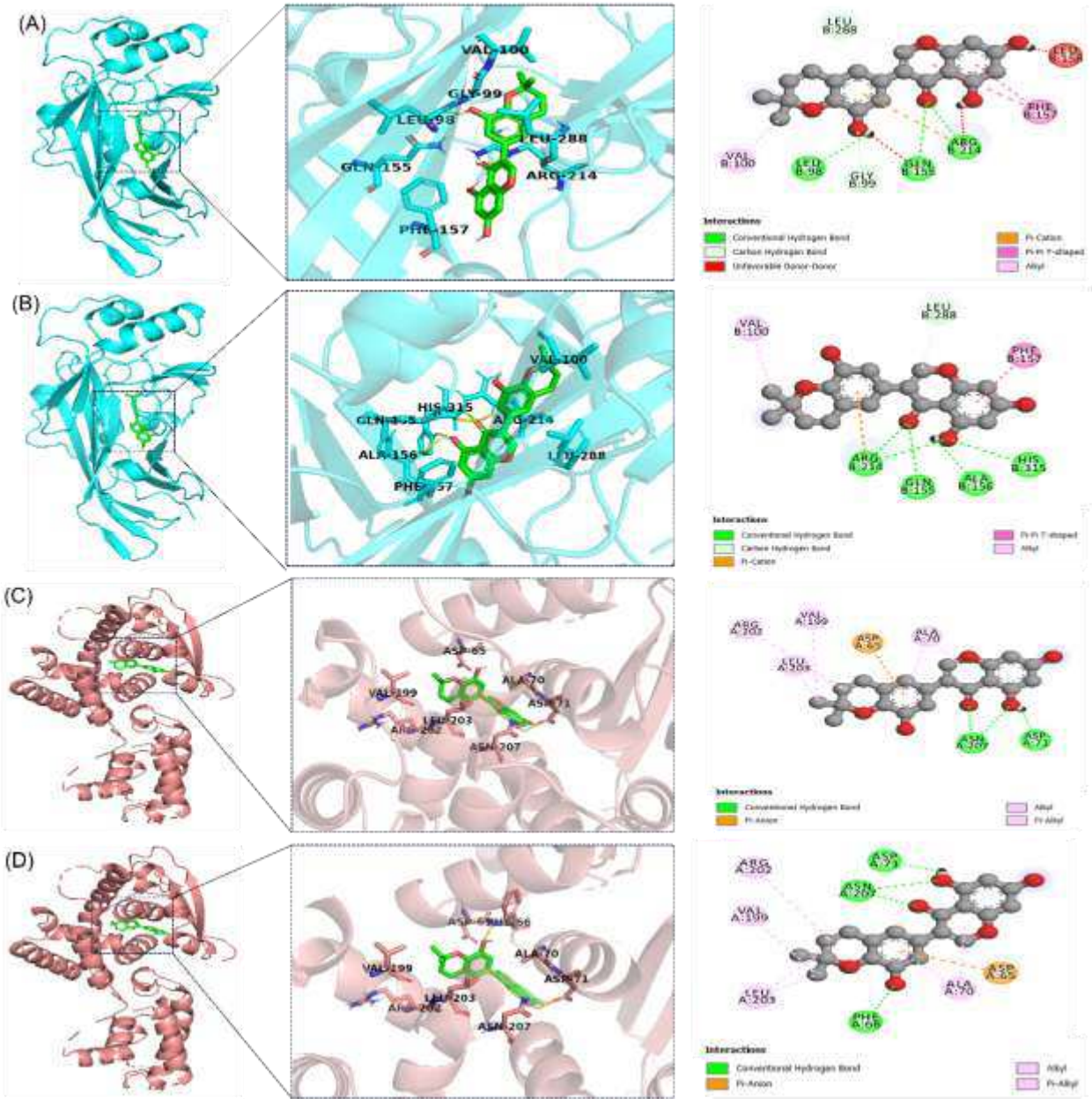


Fig. 1 Detailed visualization of protein–ligand binding interactions and corresponding two-dimensional (2D) interaction maps illustrating the binding modes of Licoisoflavone B and Semilicoisoflavone B within the active sites of Ebola virus VP40 and NP proteins. Panels (A) and (B) depict interactions with VP40, while panels (C) and (D) represent interactions with NP, highlighting key residues involved in ligand stabilization.

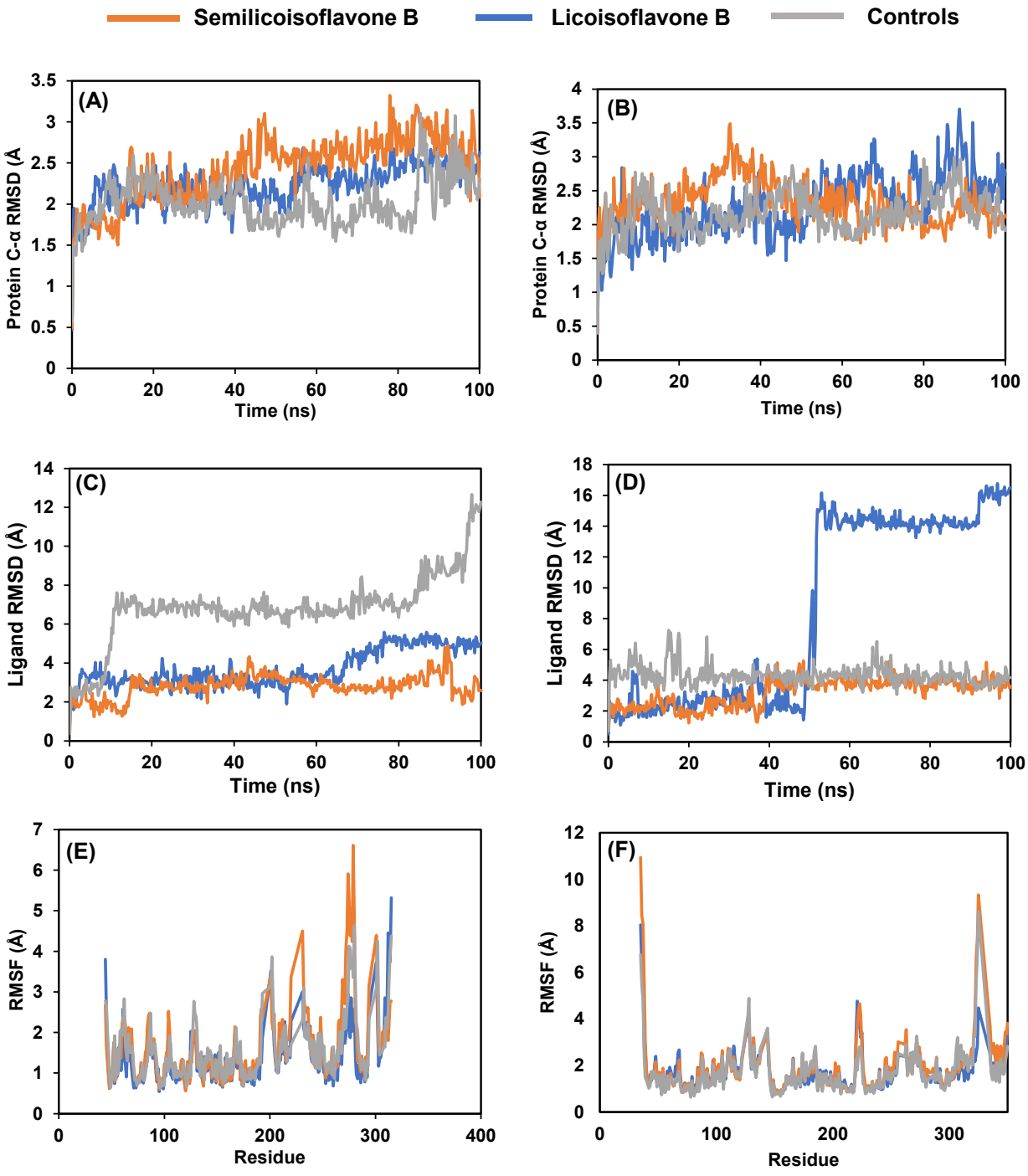


Fig. 2. Molecular dynamics-based stability and flexibility analyses of protein–ligand complexes. Time-resolved Cα backbone RMSD trajectories of (A) VP40 and (B) NP complexes, demonstrating overall structural stability during the simulation period. Ligand RMSD profiles, calculated after fitting to the protein backbone, are shown for (C) VP40 and (D) NP complexes, reflecting ligand binding stability within the active sites. Residue-wise flexibility is illustrated by

RMSF plots for (E) VP40 and (F) NP complexes, highlighting dynamic regions and key fluctuations upon ligand binding. In all panels, the orange, blue, and grey lines represent Semilicoisoflavone B, Licoisoflavone B, and the respective control ligands (Leurofoline for VP40 and Licochalcone A for NP), respectively.

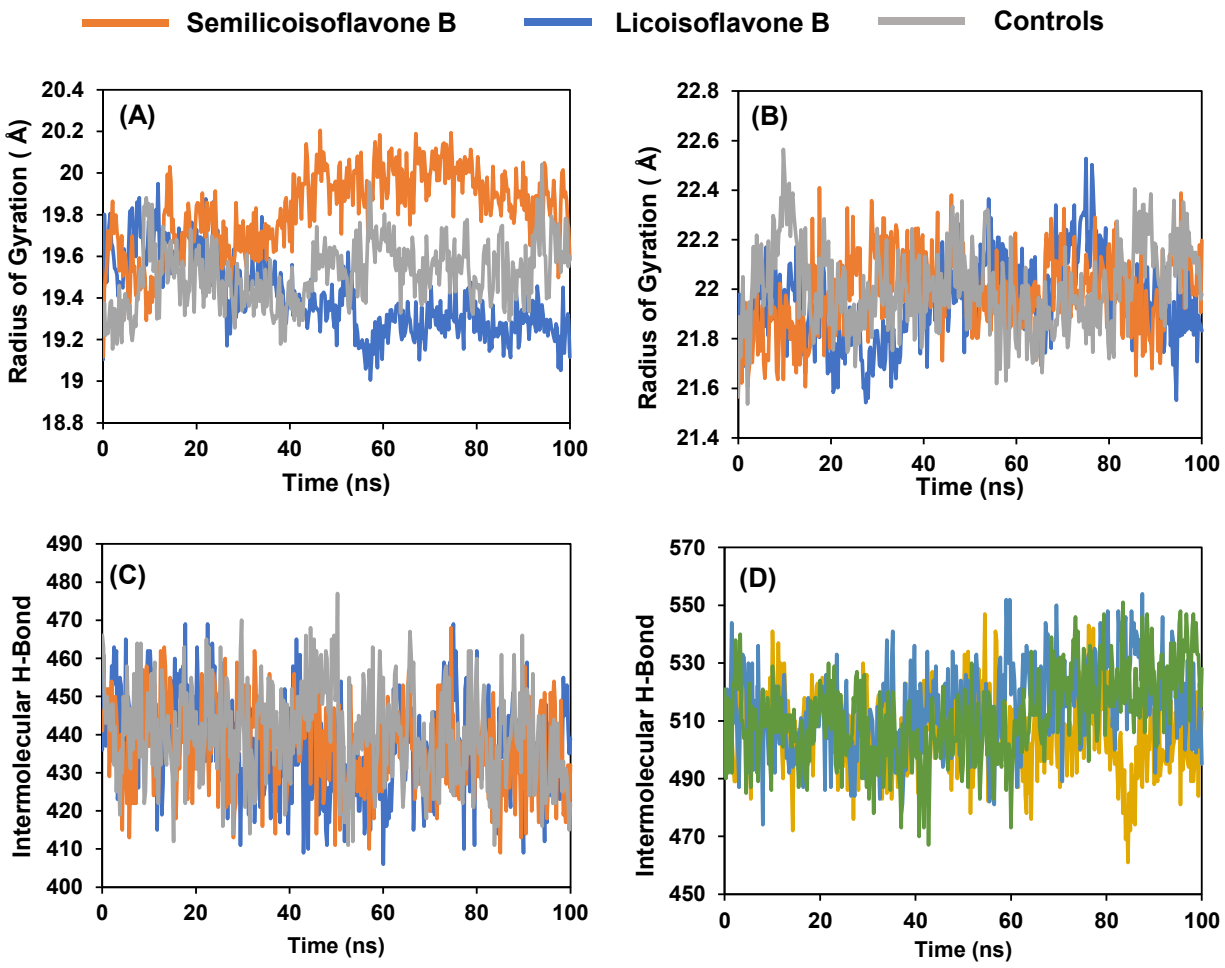


Fig. 3. Structural compactness and intermolecular interaction analysis of protein–ligand complexes during molecular dynamics simulations. Time-dependent radius of gyration (Rg) profiles for (A) VP40 and (B) NP complexes indicate overall conformational stability and compactness. The evolution of intermolecular hydrogen bonds for (C) VP40 and (D) NP complexes highlights the stability and persistence of ligand binding within the active sites. In all

panels, the orange, blue, and grey lines represent Semilicoisoflavone B, Licoisoflavone B, and the respective control ligands, respectively.

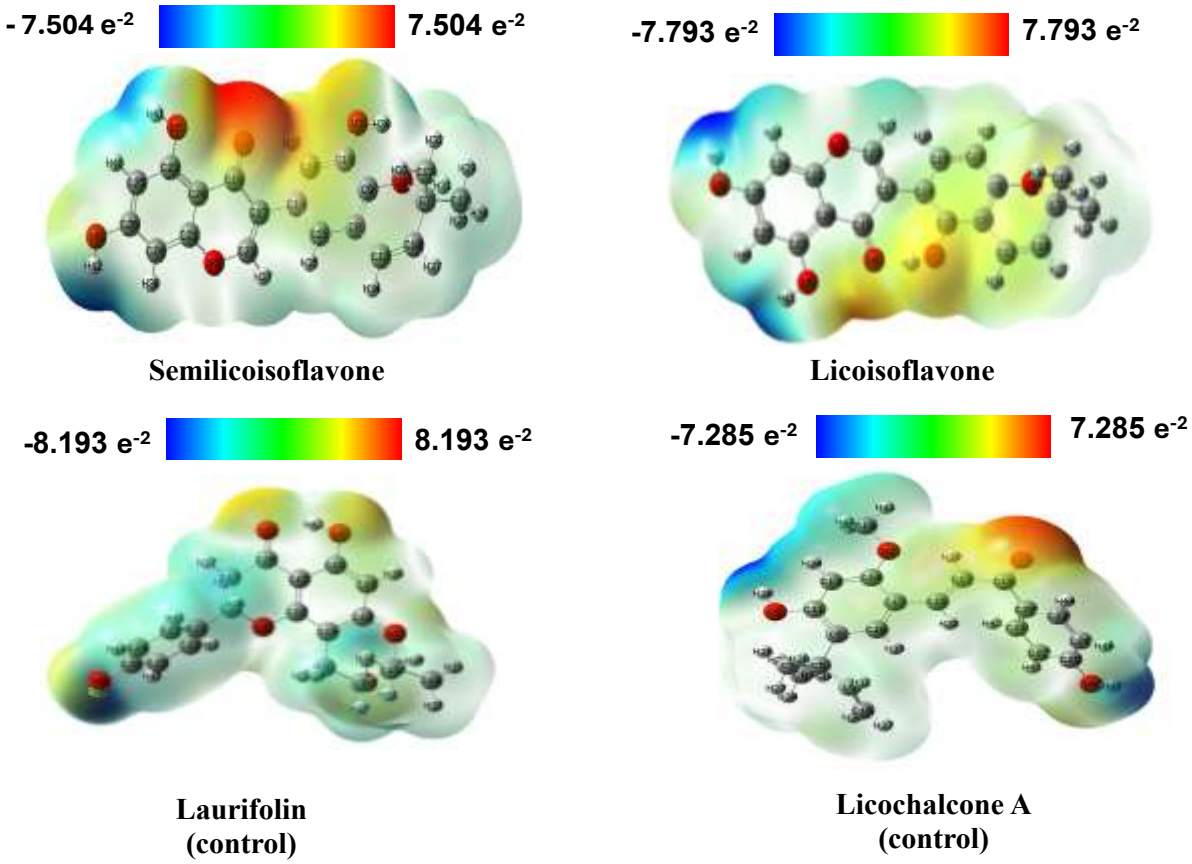
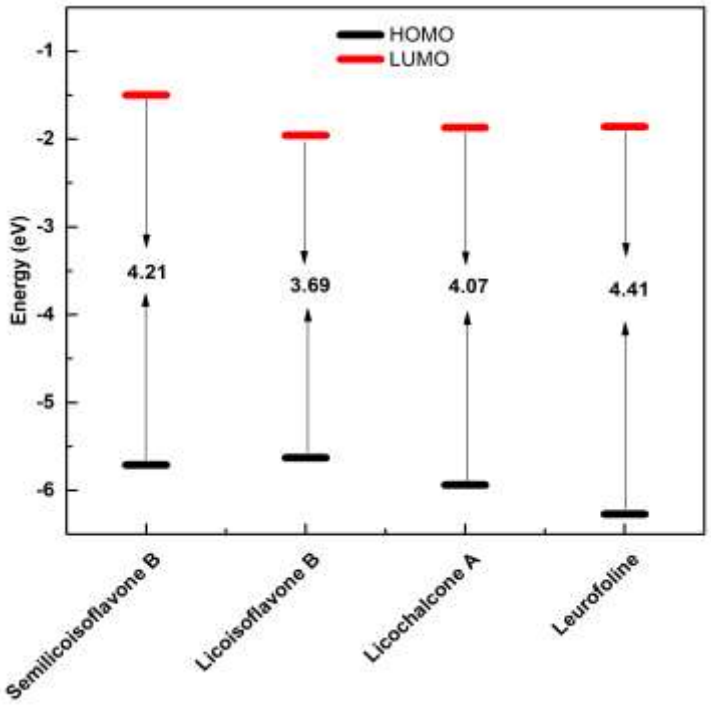


Fig. 4. Molecular electrostatic potential (MEP) surface representations of the selected lead compounds and their corresponding control molecules, illustrating the distribution of electrostatic charge across the molecular surfaces and highlighting regions of potential electrophilic and nucleophilic interactions relevant to protein binding.



739

740 **Fig. 5**. Frontier molecular orbital analysis of the selected lead compounds and their corresponding
741 control molecules, showing the highest occupied molecular orbital (HOMO), lowest unoccupied
742 molecular orbital (LUMO), and the resulting HOMO–LUMO energy gaps, which reflect the
743 chemical reactivity and stability of the compounds.

Table 1. Binding affinity scores, PubChem CID, phytochemicals, three-dimensional (3D) structures, sources, and the biological uses of these top ligands, along with corresponding control drugs, Leurofoline and Licochalcone A.

Compounds (PubChem CID)	Phytochemical	3D structure	Binding Affinity scores (kcal/mol)		Source	Biological activities
			VP40	Nucleoprotein		
CID: 5481948	Semilicoisoflavone B		-10	-9.2	*Glycyrrhiza glabra*	Neuroprotective and anti-inflammatory property [23,88]
CID: 5481234	Licoisoflavone B		-9.7	-8.8	*Glycyrrhiza glabra*	Antiviral and anti-inflammatory activity along with antioxidant potential [89]
CID: 44257868	Laurifolin (control)		-8.8	-	*Rollinia laurifolia*	Anti-diabetic, anti-tumor activity [90]
CID: 5318998	Licochalcone A (control)		-	-7.3	*Glycyrrhiza inflata*	anti-inflammatory, antimalarial and anticancer properties [28,29]

Table 2. Toxicity profiles of the selected phytocompounds using Protox-3.0 and pkCSM.

Server	Parameters	Semilicoisoflavone B	Licoisoflavone B
Protox 3.0	Hepatotoxicity	Inactive	Inactive
	Neurotoxicity	Inactive	Inactive
	Cardiotoxicity	Inactive	Inactive
	Mutagenicity	Inactive	Inactive
	Carcinogenicity	Inactive	Inactive
	Cytotoxicity	Inactive	Inactive
pkCSM	AMES Toxicity	No	No
	hERG I inhibitor	No	No
	hERG II inhibitor	No	No
	Oral Rat Acute Toxicity (LD50)	2.404	2.397
	Skin Sensitisation	No	No
	Max. tolerated dose (human)	0.488	0.502

Table 3. Mean ± standard deviation (SD) values of RMSD, RMSF, SASA, radius of gyration (Rg), and MM-PBSA binding free energy for the simulated protein–ligand complexes.

Protein–ligand complex	RMSD (Å)	RMSF (Å)	SASA (Å^2)	Rg (Å)	MM-PBSA (kcal mol^{-1})
NP-Licoisoflavone B	2.28±0.46	1.74±0.87	14270.45±228.99	21.95±0.17	-35.42±53.48
NP-Semilicoisoflavone B	2.33±0.33	1.90±1.22	14322.24±295.66	21.98±0.16	-35.74±69.23
NP-Licochalcone A (Control)	2.16±0.30	1.69±0.93	14353.32±282.47	22.01±0.17	-0.20±34.47
VP40-Licoisoflavone B	2.23±0.26	1.39±0.70	12450.66±239.94	19.41±0.19	-42.32±49.67
VP40-Semilicoisoflavone B	2.43±0.39	1.64±0.92	12653.88±179.36	19.82±0.19	-129.21±46.36
VP40-Leurofoline(control)	2.02±0.28	1.58±0.80	12745.16±212.55	19.52±0.15	-152.46±50.07

Table 4. Quantum chemical parameters of compounds calculated at the level of theory RB3LYP/6-311G + (d,p)

Name	∈LUMO	∈HOMO	Gap	(χ)	(μ)	(η)	(ω)	(S)
Semilicoisoflavone B	-5.72	-1.51	4.21	3.62	-3.62	2.10	3.11	0.24
Licoisoflavone B	-5.64	-1.96	3.69	3.80	-3.80	1.84	3.91	0.27
Leurofoline	-6.27	-1.86	4.41	4.06	-4.06	2.20	3.75	0.23
Licochalcone A	-5.94	-1.87	4.07	3.91	-3.91	2.03	3.75	0.25

Note: hardness (η), softness (S), chemical potential (μ), electronegativity (χ), and electrophilicity (ω), Chemical softness(σ)

Author contributions

Fahad Fardin: Conceptualization, Methodology, Investigation, Visualization, Validation, Writing – original draft. **MD Al-Amin:** Visualization, Investigation, Writing – original draft. **Abir Hossain:** Data curation, Formal analysis, Methodology, Writing – original draft. **Moshammat Nasrin Akter:** Data curation**,** Formal analysis**,** Methodology, Writing – original draft. **Md. Shohel Hossain:** Methodology, Writing **–** review & editing. **M. Nazmul Hoque:** Conceptualization, Supervision, Validation, Writing **–** review & editing.

Funding

This research did not receive any specific grant from funding agencies in the public, commercial, or not-for-profit sectors.

Declaration

Conflict of interest

The authors declare no conflict of interest.

Data Availability

All data generated or analyzed during this *in-silico* study are included within the article and its supplementary materials.

Reference

1 Jacob, S. T. *et al.* Ebola virus disease. *Nature reviews Disease primers* **6**, 13 (2020).

2 Malvy, D., McElroy, A. K., de Clerck, H., Günther, S. & van Griensven, J. Ebola virus disease. *The Lancet* **393**, 936-948 (2019).

3 Kuhn, J. H. *et al.* New filovirus disease classification and nomenclature. *Nature Reviews Microbiology* **17**, 261-263 (2019).

4 Baseler, L., Chertow, D. S., Johnson, K. M., Feldmann, H. & Morens, D. M. The pathogenesis of Ebola virus disease. *Annual Review of Pathology: Mechanisms of Disease* **12**, 387-418 (2017).

5 Vetter, P., Kaiser, L., Schibler, M., Ciglenecki, I. & Bausch, D. G. Sequelae of Ebola virus disease: the emergency within the emergency. *The Lancet Infectious Diseases* **16**, e82-e91 (2016).

6 Breman, J. G. *et al.* Discovery and description of Ebola Zaire virus in 1976 and relevance to the West African epidemic during 2013–2016. *The Journal of infectious diseases* **214**, S93-S101 (2016).

7 Ndayambaje, M. *et al.* Molecular characterization of Ebola virus, immune response, and therapeutic challenges: a narrative review. *Egyptian Journal of Medical Human Genetics* **25**, 133 (2024).

8 Mwamba, D. *et al.* New Ebola virus disease outbreak in the Democratic Republic of the Congo: early response guidance. *The Lancet* **406**, 1557-1558 (2025).

9 Almeida-Pinto, F., Pinto, R. & Rocha, J. Navigating the complex landscape of ebola infection treatment: A review of emerging pharmacological approaches. *Infectious diseases and therapy* **13**, 21-55 (2024).

10 Mulangu, S. *et al.* A randomized, controlled trial of Ebola virus disease therapeutics. *New England journal of medicine* **381**, 2293-2303 (2019).

11 Durante, D. *et al.* Small molecule drug discovery for Ebola virus disease. *RSC Medicinal Chemistry* **16**, 4571-4598 (2025).

12 Fujita-Fujiharu, Y. *et al.* Structural basis for Ebola virus nucleocapsid assembly and function regulated by VP24. *Nature Communications* **16**, 2171 (2025).

13 Sugita, Y., Matsunami, H., Kawaoka, Y., Noda, T. & Wolf, M. Cryo-EM structure of the Ebola virus nucleoprotein–RNA complex at 3.6 Å resolution. *Nature* **563**, 137-140 (2018).

14 Dong, S. *et al.* Insight into the Ebola virus nucleocapsid assembly mechanism: crystal structure of Ebola virus nucleoprotein core domain at 1.8 Å resolution. *Protein & cell* **6**, 351-362 (2015).

15 Stahelin, R. V. Could the Ebola virus matrix protein VP40 be a drug target? *Expert opinion on therapeutic targets* **18**, 115-120 (2014).

16 Bornholdt, Z. A. *et al.* Structural rearrangement of ebola virus VP40 begets multiple functions in the virus life cycle. *Cell* **154**, 763-774 (2013).

17 Wu, L. *et al.* The two-stage interaction of Ebola virus VP40 with nucleoprotein results in a switch from viral RNA synthesis to virion assembly/budding. *Protein & Cell* **13**, 120-140 (2022).

18 Shaikh, F. *et al.* Structure-based in silico screening identifies a potent ebolavirus inhibitor from a traditional Chinese medicine library. *Journal of medicinal chemistry* **62**, 2928-2937 (2019).
19 Mirza, M. U. *et al.* Perspectives towards antiviral drug discovery against Ebola virus. *Journal of medical virology* **91**, 2029-2048 (2019).
20 Darko, L. K. *et al.* Computational study on potential novel anti-Ebola virus protein VP35 natural compounds. *Biomedicines* **9**, 1796 (2021).
21 Siddiquee, N. H. *et al.* In-silico identification of novel natural drug leads against the Ebola virus VP40 protein: A promising approach for developing new antiviral therapeutics. *Informatics in Medicine Unlocked* **45**, 101458 (2024).
22 Nasution, M. A. F., Toepak, E. P., Alkaff, A. H. & Tambunan, U. S. F. Flexible docking-based molecular dynamics simulation of natural product compounds and Ebola virus Nucleocapsid (EBOV NP): a computational approach to discover new drug for combating Ebola. *BMC bioinformatics* **19**, 419 (2018).
23 Batiha, G. E.-S., Beshbishy, A. M., El-Mleeh, A., Abdel-Daim, M. M. & Devkota, H. P. Traditional uses, bioactive chemical constituents, and pharmacological and toxicological activities of Glycyrrhiza glabra L.(Fabaceae). *Biomolecules* **10**, 352 (2020).
24 Wang, L., Yang, R., Yuan, B., Liu, Y. & Liu, C. The antiviral and antimicrobial activities of licorice, a widely-used Chinese herb. *Acta pharmaceutica sinica B* **5**, 310-315 (2015).
25 Adianti, M. *et al.* Anti-hepatitis C virus compounds obtained from Glycyrrhiza uralensis and other Glycyrrhiza species. *Microbiology and immunology* **58**, 180-187 (2014).
26 Cinatl, J. *et al.* Glycyrrhizin, an active component of liquorice roots, and replication of SARS-associated coronavirus. *The lancet* **361**, 2045-2046 (2003).
27 Wang, Z. *et al.* Efficient ligand discovery from natural herbs by integrating virtual screening, affinity mass spectrometry and targeted metabolomics. *Analyst* **144**, 2881-2890 (2019).
28 Song, N. R. *et al.* Licochalcone A, a polyphenol present in licorice, suppresses UV-induced COX-2 expression by targeting PI3K, MEK1, and B-Raf. *International journal of molecular sciences* **16**, 4453-4470 (2015).
29 Chen, X., Liu, Z., Meng, R., Shi, C. & Guo, N. Antioxidative and anticancer properties of Licochalcone A from licorice. *Journal of ethnopharmacology* **198**, 331-337 (2017).
30 Paul, A., Vibhuti, A. & Raj, S. Molecular docking NS4B of DENV 1-4 with known bioactive phyto-chemicals. *Bioinformation* **12**, 140 (2016).
31 Ma, Z., Ajibade, A. & Zou, X. Docking strategies for predicting protein-ligand interactions and their application to structure-based drug design. *Communications in information and systems* **24**, 199 (2024).
32 Islam, M. A. *et al.* In-silico study unveils potential phytocompounds in Andrographis paniculata against E6 protein of the high-risk HPV-16 subtype for cervical cancer therapy. *Scientific Reports* **14**, 17182 (2024).

33 Biswas, S. *et al.* In-silico characterization of deleterious non-synonymous SNPs in the human S1PR1 gene reveals structural instability and altered ligand affinity. *PLoS One* **21**, e0339370 (2026).

34 Hossain, M. S. *et al.* Computational identification of Vernonia cinerea-derived phytochemicals as potential inhibitors of nonstructural protein 1 (NSP1) in dengue virus serotype-2. *Frontiers in Pharmacology* **15**, 1465827 (2024).

35 Elsaman, T. *et al.* Pharmacophore-based virtual screening and in silico investigations of small molecule library for discovery of human hepatic ketohexokinase inhibitors for the treatment of fructose metabolic disorders. *Frontiers in Pharmacology* **16**, 1531512 (2025).

36 Lee, J., Beers, J. L., Geffert, R. M. & Jackson, K. D. A review of CYP-mediated drug interactions: mechanisms and in vitro drug-drug interaction assessment. *Biomolecules* **14**, 99 (2024).

37 Furutani, K. Facilitation of hERG activation by its blocker: A mechanism to reduce Drug-Induced proarrhythmic risk. *International Journal of Molecular Sciences* **24**, 16261 (2023).

38 Hossen, M. A. *et al.* Computational investigation unveils pathogenic LIG3 non-synonymous mutations and therapeutic targets in acute myeloid leukemia. *Plos one* **20**, e0320550 (2025).

39 Hasnat, S. *et al.* High throughput screening identifies potential inhibitors targeting trimethoprim resistant DfrA1 protein in Klebsiella pneumoniae and Escherichia coli. *Scientific Reports* **15**, 7141 (2025).

40 Zare, F. *et al.* A combination of virtual screening, molecular dynamics simulation, MM/PBSA, ADMET, and DFT calculations to identify a potential DPP4 inhibitor. *Scientific Reports* **14**, 7749 (2024).

41 Waiba, A. *et al.* Computational insights into flavonoids inhibition of dengue virus envelope protein: ADMET profiling, molecular docking, dynamics, PCA, and end-state free energy calculations. *Plos one* **20**, e0327862 (2025).

42 Boreak, N. *et al.* Molecular docking and MD simulations predicted quercetin as a potent human interleukin-1 beta (hIL1β) inhibitor for improved endodontic disease management. *Plos one* **20**, e0336841 (2025).

43 Uddin, M. M. *et al.* Molecular screening and dynamics simulation reveal potential phytocompounds in Swertia chirayita targeting the UspA1 protein of Moraxella catarrhalis for COPD therapy. *Plos one* **20**, e0316275 (2025).

44 Rahman, M. S. *et al.* Epitope-based chimeric peptide vaccine design against S, M and E proteins of SARS-CoV-2, the etiologic agent of COVID-19 pandemic: an in silico approach. *PeerJ* **8**, e9572 (2020).

45 Khan, M. A. A. M. *et al.* In-silico prediction of highly promising natural fungicides against the destructive blast fungus Magnaporthe oryzae. *Heliyon* **9** (2023).

46 David, C. C. & Jacobs, D. J. in *Protein dynamics: Methods and protocols* 193-226 (Springer, 2013).

47 Ali, M. Y. *et al.* Identification and in silico evaluation of natural compounds from Annona muricata (soursop) leaves for colon cancer treatment. *Scientific Reports* (2025).

48 Feizi-Dehnayebi, M. *et al.* Biological evaluations and biomolecular interactions along with computational insights of arylidene isatin hydrazones synthesized using nanocatalyst. *Scientific Reports* **15**, 42705 (2025).
49 Elsayed, G. H. & Fahim, A. M. Multifunctional pectin derivatives as anticancer agents in colorectal cancer via synthesis, computational insights, and modulation of NRF2/HO-1, HIF-1α, and VEGF/PDGF-D signaling pathways. *Scientific Reports* (2026).
50 Kaplan, W. & Littlejohn, T. G. Swiss-PDB viewer (deep view). *Briefings in bioinformatics* **2**, 195-197 (2001).
51 Mohanraj, K. *et al.* IMPPAT: A curated database of Indian Medicinal Plants, Phytochemistry And Therapeutics. *Scientific Reports* **8**, 4329 (2018). https://doi.org:10.1038/s41598-018-22631-z
52 Vivek-Ananth, R., Mohanraj, K., Sahoo, A. K. & Samal, A. IMPPAT 2.0: an enhanced and expanded phytochemical atlas of Indian medicinal plants. *ACS omega* **8**, 8827-8845 (2023).
53 Kim, S. *et al.* PubChem 2025 update. *Nucleic acids research* **53**, D1516-D1525 (2025).
54 Laxmi, K. Characterization of Ligand N'-[(1E)-1-phenylethylidene]-1, 3-benzothiazole-2-carbohydrazide by using Marvin Sketch 20.8 Software. *Oriental Journal Of Chemistry* **38** (2022).
55 Hanwell, M. D. *et al.* Avogadro: an advanced semantic chemical editor, visualization, and analysis platform. *Journal of cheminformatics* **4**, 17 (2012).
56 Pawar, R. P. & Rohane, S. H. Role of autodock vina in PyRx molecular docking. *Asian Journal of Research in Chemistry* **14**, 132-134 (2021).
57 Huey, R., Morris, G. M. & Forli, S. Using AutoDock 4 and AutoDock vina with AutoDockTools: a tutorial. *The Scripps Research Institute Molecular Graphics Laboratory* **10550**, 1000 (2012).
58 Vina, A. Improving the speed and accuracy of docking with a new scoring function, efficient optimization, and multithreading Trott, Oleg; Olson, Arthur J. *J. Comput. Chem* **31**, 455-461 (2010).
59 Baroroh, U. *et al.* Molecular interaction analysis and visualization of protein-ligand docking using Biovia Discovery Studio Visualizer. *Indonesian Journal of Computational Biology (IJCB)* **2**, 22-30 (2023).
60 Yusuf, D., Davis, A. M., Kleywegt, G. J. & Schmitt, S. An alternative method for the evaluation of docking performance: RSR vs RMSD. *Journal of chemical information and modeling* **48**, 1411-1422 (2008).
61 Cheng, F. *et al.* (ACS Publications, 2012).
62 Lipinski, C. A. Lead-and drug-like compounds: the rule-of-five revolution. *Drug discovery today: Technologies* **1**, 337-341 (2004).
63 Veber, D. F. *et al.* Molecular properties that influence the oral bioavailability of drug candidates. *Journal of medicinal chemistry* **45**, 2615-2623 (2002).
64 Muegge, I. Selection criteria for drug-like compounds. *Medicinal research reviews* **23**, 302-321 (2003).

65 Egan, W. J., Merz, K. M. & Baldwin, J. J. Prediction of drug absorption using multivariate statistics. *Journal of medicinal chemistry* **43**, 3867-3877 (2000).
66 Lipinski, C. A., Lombardo, F., Dominy, B. W. & Feeney, P. J. Experimental and computational approaches to estimate solubility and permeability in drug discovery and development settings. *Advanced drug delivery reviews* **23**, 3-25 (1997).
67 Pires, D. E., Blundell, T. L. & Ascher, D. B. pkCSM: predicting small-molecule pharmacokinetic and toxicity properties using graph-based signatures. *Journal of medicinal chemistry* **58**, 4066-4072 (2015).
68 Banerjee, P., Eckert, A. O., Schrey, A. K. & Preissner, R. ProTox-II: a webserver for the prediction of toxicity of chemicals. *Nucleic acids research* **46**, W257-W263 (2018).
69 Allouche, A. R. Gabedit—A graphical user interface for computational chemistry softwares. *Journal of computational chemistry* **32**, 174-182 (2011).
70 Taha, D. K., Hilal, I. H. & Jabbar, R. H. in *Journal of physics: Conference series*. 012054 (IOP Publishing).
71 Ahmad, I., Jagatap, V. & Patel, H. in *Phytochemistry, computational tools and databases in drug discovery* 371-392 (Elsevier, 2023).
72 Kruse, H., Goerigk, L. & Grimme, S. Why the standard B3LYP/6-31G* model chemistry should not be used in DFT calculations of molecular thermochemistry: understanding and correcting the problem. *The Journal of organic chemistry* **77**, 10824-10834 (2012).
73 Hossain, M. A. *et al*. Genome-Wide Investigation Reveals Potential Therapeutic Targets in Shigella spp. *BioMed Research International* **2024**, 5554208 (2024).
74 Politzer, P. & Murray, J. S. The fundamental nature and role of the electrostatic potential in atoms and molecules. *Theoretical Chemistry Accounts* **108**, 134-142 (2002).
75 Vijayakumar, S. & Wilmouth, D. M. Kinetics of the Reactions of Chlorinated Very Short-Lived Substances (VSLSs) with Chlorine Atoms. *The Journal of Physical Chemistry A* **127**, 7284-7294 (2023).
76 Hasnat, S. *et al*. High-Throughput Screening Reveals Potential Inhibitors Targeting Trimethoprim-Resistant DfrA1 Protein in Klebsiella pneumoniae and Escherichia coli. *bioRxiv*, 2024.2011. 2018.624070 (2024).
77 Krieger, E. & Vriend, G. YASARA View—molecular graphics for all devices—from smartphones to workstations. *Bioinformatics* **30**, 2981-2982 (2014).
78 Bhadra, P. & Siu, S. W. Refined empirical force field to model protein–self-assembled monolayer interactions based on AMBER14 and GAFF. *Langmuir* **35**, 9622-9633 (2019).
79 Jorgensen, W. L., Chandrasekhar, J., Madura, J. D., Impey, R. W. & Klein, M. L. Comparison of simple potential functions for simulating liquid water. *The Journal of chemical physics* **79**, 926-935 (1983).
80 Wang, H., Dommert, F. & Holm, C. Optimizing working parameters of the smooth particle mesh Ewald algorithm in terms of accuracy and efficiency. *The Journal of chemical physics* **133** (2010).

81 Martínez, L. Automatic identification of mobile and rigid substructures in molecular dynamics simulations and fractional structural fluctuation analysis. *PloS one* **10**, e0119264 (2015).
82 Abdullah, M. & Khairurrijal, K. A simple method for determining surface porosity based on SEM images using OriginPro software. *Indonesian Journal of Physics* **20**, 37-40 (2009).
83 Kollman, P. A. *et al.* Calculating structures and free energies of complex molecules: combining molecular mechanics and continuum models. *Accounts of chemical research* **33**, 889-897 (2000).
84 Wang, C., Greene, D. A., Xiao, L., Qi, R. & Luo, R. Recent developments and applications of the MMPBSA method. *Frontiers in molecular biosciences* **4**, 87 (2018).
85 Genheden, S. & Ryde, U. The MM/PBSA and MM/GBSA methods to estimate ligand-binding affinities. *Expert opinion on drug discovery* **10**, 449-461 (2015).
86 Adamo, C. & Jacquemin, D. The calculations of excited-state properties with Time-Dependent Density Functional Theory. *Chemical Society Reviews* **42**, 845-856 (2013).
87 Andersson, M. P. & Uvdal, P. New scale factors for harmonic vibrational frequencies using the B3LYP density functional method with the triple-ζ basis set 6-311+ G (d, p). *The Journal of Physical Chemistry A* **109**, 2937-2941 (2005).
88 Gu, M. Y., Chun, Y. S., Zhao, D., Ryu, S. Y. & Yang, H. O. Glycyrrhiza uralensis and semilicoisoflavone B reduce Aβ secretion by increasing PPARγ expression and inhibiting STAT3 phosphorylation to inhibit BACE1 expression. *Molecular nutrition & food research* **62**, 1700633 (2018).
89 Toda, S. & Shirataki, Y. Inhibitory effects of licoisoflavones a and b and sophoraisoflavone a of Sophra mooracroftiana Beth ex baker on copper-ion-induced protein oxidative modification of mice brain homogenate, in vitro. *Biological Trace Element Research* **81**, 169-175 (2001).
90 Muhammad, A. J. *et al.* Determination of antioxidant and α–amylase inhibition properties of Alligator pepper (Aframomum Melegueta): a potential therapeutic against Diabetes Mellitus. *EAS J. Pharm. Pharmacol* **4**, 43-42 (2022).

Supplementary Files

This is a list of supplementary files associated with this preprint. Click to download.

- SupplementaryMaterials.docx